Synthesis, structural and electrical characterization of a new organic inorganic bromide: [(C3H7)4N]2CoBr4

M. Khalfa, A. Oueslati, K. Khirouni, M. Gargouri, A. Rousseau, J. Lhoste, Jean-François Bardeau, G. Corbel

RSC Advances

PAPER

View Article Online
View Journal | View Issue

Cite this: *RSC Adv.*, 2022, **12**, 2798

Synthesis, structural and electrical characterization of a new organic inorganic bromide: $[(C_3H_7)_4N]_2CoBr_4$†

M. Khalfa, *[a] A. Oueslati, [b] K. Khirouni,[a] M. Gargouri,[b] A. Rousseau,[c] J. Lhoste, [c] J.-F. Bardeau[c] and G. Corbel [c]

A new organic inorganic hybrid $[TPA]_2CoBr_4$, where TPA = $[(C_3H_7)_4N]^+$ (*i.e.*, tetra-propyl-ammonium) compound has been synthesized by slow evaporation method at room temperature. Single crystal X-ray diffraction (SC-XRD), X-ray powder diffraction (XRPD), thermal analyses, vibrational and complex impedance spectroscopy have been used to characterize both structural, thermal, electrical properties. $[TPA]_2CoBr_4$ crystallizes in the monoclinic system (*C*2/*c* space group) with the following cell parameters: a = 33.145 (5) Å, b = 14.234 (3) Å, c = 15.081 (2) Å and β = 110.207 (5)°. In the crystal structure, the organic TPA cations which form layers stacked along the *a*-axis, are separated from each other by inorganic tetrahedral $[CoBr_4]^{2-}$ anions. The XRPD pattern confirms both the high purity of the sample and the crystalline nature of the powder. The differential scanning calorimetry (DSC) analysis shows an endothermic peak at 394 K upon heating which is ascribed to a structural phase transition since no decomposition of the titled compound is evidenced by thermogravimetric analysis. The ac conductivity and the dielectric properties confirm the presence of the phase transition. At the structural phase transition around 394 K, a change from a quantum mechanical tunneling to a correlated barrier hopping conduction models is determined from the temperature dependence of the exponent s of the Jonscher's power law. The analysis of complex impedance spectra shows that the electrical properties of the material are heavily dependent on frequency and temperature, indicating a relaxation phenomenon and semiconductor-type behavior. One single semicircle is detectable in the Nyquist plots of the complex impedance spectra which can be satisfactorily fitted with a combination *R*//CPE elements assigned to the bulk response. This behavior suggests that the sample is electrically homogeneous. Capacitance analysis proves the high effective permittivity at radio frequencies in the sample.

Received 29th October 2021
Accepted 4th January 2022

DOI: 10.1039/d1ra07965d

rsc.li/rsc-advances

1. Introduction

In recent years, research on organic–inorganic hybrid materials has had a great expansion due to the fascinating opportunities for the preparation of a large variety of materials and the diversity of physicochemical properties which leads to a broad range of applications for treating wastewater, optical devices, information storage, solar cell, photocatalyst, thin film transistor, *etc.*[1–3] Physical properties of stimuli-responsive materials are highly sensitive to external stimuli such as temperature, light, pressure, electric and magnetic fields, *etc.*[4–7] In particular, the switching of bulk properties between at least two distinct states through multiple physical paths has potential applications as sensors, signal processing and memory devices.[8,9] Among them, switchable dielectric compounds, whose dielectric constants can be converted between low and high states, have taken an emerging position in the field of stimuli responsive materials. Temperature behaves as the most frequently used and easily controlled trigger. In this context, thermal induced phase transition compounds have afforded great potentials as promising switchable dielectrics, and their physical responses display abrupt changes in the vicinity of phase transition. In particular, the hybrid compounds with general formula R_2MX_4 (R: tetra-alkylammonium cations = $((C_nH_{2n+1})_4N$ where n = 1, 2, 3); M: metal = Fe, Co, Cu, Mn, Cd… and X: halogen = Cl, Br, I) show many structural transitions of the order–disorder type, due to reorientation/displacements of tetra-alkylammonium cations.[10–13] Several compounds incorporating tetra-propyl-ammonium (TPA) cations have already been reported in literature such as $[TPA]_2CuI_4$,[14] $[TPA]_2CoCl_4$.[15]

[a]*Laboratoire de Physique des Matériaux et des Nanomatériaux appliquée à l'Environnement, Faculté des Sciences de Gabès cité Erriadh, 6079 Gabès, Tunisia. E-mail: maryemkhalfa28@gmail.com*

[b]*Laboratory for Spectroscopic Characterization and Optics of Materials, Faculty of Sciences, University of Sfax, B. P. 1171, 3000 Sfax, Tunisia*

[c]*Institut des Molécules et Matériaux du Mans (IMMM), UMR-6283 CNRS, Le Mans Université, Avenue Olivier Messiaen, 72085 Le Mans Cedex 9, France*

† CCDC 2087968 and atomic coordinates anisotropic, displacement parameters, tables for all bond distances, and angles. For crystallographic data in CIF or other electronic format see DOI: 10.1039/d1ra07965d

They have special interest because of their specific properties (nonlinear optical activity, semiconductor behavior, ferroelectric and ferroelastic properties…).[16,17]

Special attention is paid to compounds where tetrahedral coordination of divalent cobalt by anions leads to interesting electrical properties. Indeed, the tetrahedral crystal field splits the five d-orbitals of the divalent cobalt ion into two sets. The doubly degenerate e-orbitals are stabilized while the triply degenerate t_2 orbitals are destabilized relative to their energies in a spherical field. For the d^7 electronic configuration of Co^{2+} ion, the e-orbitals are fully occupied, whereas equal occupancies of the three t_2 orbitals are noted (*i.e.* $(e)^4(t_2)^3$ with three unpaired electrons).[18] Surprisingly, the bromine analogue of $[TPA]_2CoCl_4$ has never been synthesized or characterized. This study aims to fill this gap.

The new $[TPA]_2CoBr_4$ compound has therefore been prepared with the aim of studying its thermal, vibrational and electrical properties by using thermogravimetric and differential thermal analyses (TGA-DTA), differential scanning calorimetry (DSC), Raman spectroscopy and complex impedance spectroscopy, respectively. Its crystal structure was determined from X-ray diffraction data collected on a single crystal obtained by the slow evaporation method.

2. Experimental details

The synthesis of the $[TPA]_2CoBr_4$ compound was carried out using the reported preparation procedure[19,20] used for other hybrid compounds. $[(C_3H_7)_4N\ Br]$ (purity 98%, FLUKA) and $CoBr_2$ (purity 98%, FLUKA) were dissolved in distilled water. The corresponding chemical reaction is:

$$2\left[(C_3H_7)_4NBr\right] + CoBr_2 \xrightarrow{H_2O} \left[(C_3H_7)_4N\right]_2CoBr_4$$

The solution is kept at room temperature and after slow evaporation for 7 days, micrometric blue crystals begin to appear.

The phase purity was first checked on crushed crystals by recording X-ray powder diffraction (XRPD) pattern at room temperature on a Panalytical $\theta/2\theta$ Bragg–Brentano Empyrean diffractometer (using Cu $K\alpha_{1+2}$ radiations) equipped with the PIXcel^{1D} detector. XRPD pattern was collected in the [5–100°] scattering angle range, with a 0.0131° step size, for a total acquisition time of 10 h.

Prior to any crystal structure determination, micrographs were collected on several crystals with a JEOL JSM-6510LV scanning electron microscope (SEM). To obtain high quality micrographs, a thin gold film was sputtered with a JEOL JFC 1200 fine coater on few crystals randomly spread on a carbon tape. These SEM images displayed in Fig. 1 show that the average size of crystals is ranging from ≈700 to 1500 nm. Sometimes, two crystals simultaneously grow in two directions from one twin boundary, thus forming V-shape twinned crystals as observed in Fig. 1. An OXFORD Energy Dispersive X-ray Spectrometer (EDS) coupled to the microscope was also employed to verify the presence of Co, Br, C and N elements and their spatial distributions within the crystals. The distribution of these four elements is homogeneous as shown in EDS elemental maps displayed in Fig. 1. The crystals correspond to an organic cobalt bromide whose structure was then determined from X-ray diffraction data collected on a single crystal.

Crystals were selected under polarizing optical microscope and mounted on MicroMount needles (MiTiGen) for single-crystal X-ray diffraction experiments. X-ray intensity data were collected on a Bruker APEX II Quazar diffractometer (4 circle Kappa goniometer, CCD detector) using Iμs microfocus source (Mo-K_α radiation with $\lambda = 0.71073$ Å) at 296 K. The structure solutions were obtained by direct methods, developed by successive difference Fourier syntheses, and refined by full-matrix least-squares on all F^2 data using SHELX program suite in Bruker APEX2 interface. A summary of the measurements, isotropic and anisotropic displacement parameters is represented in Tables 1–3, respectively.

Atomic coordinates anisotropic, displacement parameters, tables for all bond distances, and angles have been deposited.

The thermogravimetric and differential thermal analyses were simultaneously performed on 20 mg of crushed blue crystals with a TGA/DTA Q600 SDT TA Instruments apparatus (Pt crucibles, α-Al_2O_3 as a reference) under N_2 flow (100 ml min^{-1}) from the room temperature (RT) to 423 K range (heating/cooling rate of 5 K min^{-1}). The differential scanning calorimetry (DSC) curve was recorded from 163 K to 423 K on a Sirius NETZSCH DSC 3500 analyser equipped with a liquid N_2 cooling system by heating at 10 K min^{-1}, using about 7 mg of crushed blue crystals in a closed aluminium crucible.

The Raman spectrum was recorded at room temperature, in the wavenumber range 10–3600 cm^{-1}, with a WITec Alpha 300R confocal Raman spectrometer (WITec GmbH, Ulm Germany). Raman scattered signal was collected under a microscope equipped with a Zeiss EC Epiplan-Neofluar® 50× objective (numerical aperture of 0.5) focusing the 532 nm line of a Solid-State Sapphire laser (Coherent INC., Santa Clara, USA) on the samples. The laser power was fixed to 5 mW on the sample and the integration time was 30 s.

The infrared spectrum was examined at room temperature using a PerkinElmer FT-IR 1000 spectrometer with the sample

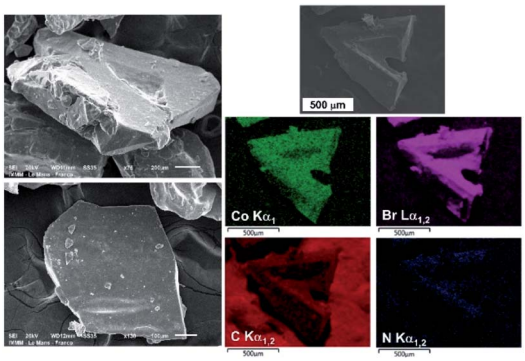

Fig. 1 SEM images of large $[(C_3H_7)_4N]_2CoBr_4$ crystals grown by slow evaporation method at room temperature and EDS elemental Co, Br, C and N maps collected on two V-shape twinned crystals.

Table 1 Crystallographic data of $[TPA]_2CoBr_4$ with TPA= $(C_3H_7)_4N^+$

Compound	$CoBr_4N_2C_{24}H_{56}$
CCDC number	2087968
M (g mol^{-1})	751.3
Crystal system	Monoclinic
ρ_{calc} (g cm^{-3})	1.492
Space group	$C2/c$
a (Å)	33.179(7)
b (Å)	14.251(3)
c (Å)	15.092(3)
β (°)	110.281(5)
V (Å^3)	6693(2)
Z	8
Wavelength (Å)	MoK_α
2θ range (°)	4.0–55.0
Limiting indices	$-43 \le h \le 42$
	$-18 \le k \le 18$
	$-15 \le l \le 19$
μ(Mo, Kα) (mm^{-1})	5.30
F(000)	2936
No. of unique reflns	7670
No. of obsd reflns [$I > 2\sigma(I)$]	4072
Parameters	283
GOF	0.997
Final R indices [$I > 2\sigma(I)$]	$R_1 = 0.0473$, $wR_2 = 0.1059$
R indices (all data)	$R_1 = 0.1181$, $wR_2 = 0.1330$
Largest diff. peak and hole (e Å^{-3})	−0.602, 0.652

pressed in spectroscopically pure KBr pellets, over the wavenumber range (400–3500 cm^{-1}). The spectral resolution was typically 4 cm^{-1}.

In order to carry out electrical measurements, the powder, resulting from the grinding of the crystals, was shaped as a pellet (≈8 mm in diameter and 1.3 mm in thickness) in a uniaxial hydraulic press at a pressure of 3 tons per cm^2. The pellet was prepared with a relative density of 94% (with respect to the theoretical absolute value calculated from X-ray diffraction data). Then, thin gold films, (with a thickness of a few nanometers), were manually deposited on both flat faces of the pellet.

The coated pellet was then placed between two platinum electrodes for electrical measurements. The complex impedance spectra were measured, in the frequency range 100 Hz–1 MHz, by using a TEGAM 3550 ALF automatic bridge monitored by a microcomputer upon heating from 343 to 418 K.

3. Results and discussion

3.1. Structure description

The single crystal X-ray diffraction shows that $[TPA]_2CoBr_4$ compound crystallized in the monoclinic system ($C2/c$ space group) with the following unit cell dimensions: $a = 33.179(7)$ Å, $b = 14.251(3)$ Å, $c = 15.092(3)$ Å, $\beta = 110.281(5)°$ and $Z = 8$. Fig. 2 and 3 show that the structure of $[TPA]_2CoBr_4$ is built up from tetrapropylammonium cations ($[(C_3H_7)_4N]^+$) and cobalt tetrabromide anions ($[CoBr_4]^-$).

The structural arrangement indicates that the organic cations form layers stacked along the a-axis and separated by

Table 2 Atomic coordinates and equivalent isotropic displacement parameters of $[TPA]_2CoBr_4$

Atom	x	y	z	U_{eq} (Å^2)
Co(1)	0.87181(2)	0.74661(5)	0.40124(5)	0.0547(2)
Br(1)	0.92105(2)	0.66100(4)	0.34313(4)	0.07237(19
Br(2)	0.80904(2)	0.80317(5)	0.27453(4)	0.0822(2)
Br(3)	0.90868(2)	0.87700(4)	0.49744(5)	0.0834(2)
Br(4)	0.84604(2)	0.64364(5)	0.49597(5)	0.0847(2)
N(1)	1/2	0.4088(4)	0.250000	0.0501(13)
C(1)	0.49200(16)	0.3460(3)	0.1647(3)	0.0544(12)
H(1)A	0.516023	0.303014	0.177629	0.065
H(1)B	0.466567	0.308716	0.157147	0.065
C(2)	0.4860(2)	0.3945(4)	0.0724(3)	0.0710(15)
H(2)A	0.511963	0.428499	0.077015	0.085
H(2)B	0.462669	0.439344	0.059143	0.085
C(3)	0.4759(2)	0.3238(5)	−0.0075(4)	0.0842(18)
H(3)A	0.498706	0.278429	0.006447	0.126
H(3)B	0.473361	0.355640	−0.065240	0.126
H(3)C	0.449423	0.292485	−0.014224	0.126
C(4)	0.53847(15)	0.4719(3)	0.2626(4)	0.0580(13)
H(4)A	0.531758	0.512540	0.207823	0.070
H(4)B	0.542451	0.511563	0.317159	0.070
C(5)	0.58072(17)	0.4229(4)	0.2754(4)	0.0767(16)
H(5)A	0.590006	0.388214	0.334338	0.092
H(5)B	0.576865	0.378639	0.224217	0.092
C(6)	0.61424(19)	0.4936(5)	0.2762(5)	0.099(2)
H(6)A	0.605057	0.527463	0.217550	0.148
H(6)B	0.640811	0.462004	0.283955	0.148
H(6)C	0.618340	0.536607	0.327497	0.148
N(2)	0.75370(12)	0.4869(3)	0.5945(2)	0.0472(9)
C(7)	0.77817(18)	0.5552(3)	0.6702(3)	0.0626(13)
H(7)A	0.803217	0.576172	0.656553	0.075
H(7)B	0.760125	0.609653	0.666575	0.075
C(8)	0.7929(2)	0.5186(5)	0.7699(4)	0.0889(19)
H(8)A	0.810133	0.462633	0.774345	0.107
H(8)B	0.768098	0.501693	0.786483	0.107
C(9)	0.8190(3)	0.5916(6)	0.8380(5)	0.144(4)
H(9)A	0.841842	0.613057	0.817688	0.216
H(9)B	0.830964	0.564580	0.899904	0.216
H(9)C	0.800902	0.643531	0.839726	0.216
C(10)	0.78013(18)	0.3982(3)	0.5980(4)	0.0659(14)
H(10)A	0.779413	0.360336	0.650821	0.079
H(10)B	0.766144	0.362461	0.540865	0.079
C(11)	0.82613(18)	0.4121(4)	0.6073(4)	0.0729(15)
H(11)A	0.842272	0.433815	0.670639	0.088
H(11)B	0.827906	0.460018	0.563130	0.088
C(12)	0.8457(2)	0.3228(4)	0.5882(4)	0.0824(18)
H(12)A	0.841967	0.274012	0.628618	0.124
H(12)B	0.875760	0.332251	0.600428	0.124
H(12)C	0.831762	0.304927	0.523400	0.124
C(13)	0.74434(15)	0.5315(3)	0.4984(3)	0.0536(12)
H(13)A	0.771580	0.545987	0.491053	0.064
H(13)B	0.730011	0.485244	0.450808	0.064
C(14)	0.71757(18)	0.6190(4)	0.4779(4)	0.0695(15)
H(14)A	0.731212	0.666481	0.524699	0.083
H(14)B	0.689512	0.605540	0.481468	0.083
C(15)	0.71252(19)	0.6552(4)	0.3803(4)	0.0793(17)
H(15)A	0.740374	0.664896	0.375836	0.119
H(15)B	0.697080	0.713507	0.369538	0.119
H(15)C	0.696894	0.610162	0.333798	0.119
C(16)	0.71279(18)	0.4598(4)	0.6103(4)	0.0695(15)
H(16)A	0.720558	0.430011	0.671785	0.083
H(16)B	0.697368	0.516932	0.613063	0.083
C(17)	0.6830(2)	0.3970(5)	0.5405(5)	0.102(2)
H(17)A	0.698228	0.340842	0.533687	0.122

Table 2 (*Contd.*)

Atom	*x*	*y*	*z*	U_{eq} (Å^2)
H(17)B	0.672327	0.428167	0.479694	0.122
C(18)	0.6451(2)	0.3697(4)	0.5715(5)	0.098(2)
H(18)A	0.655734	0.339008	0.631848	0.147
H(18)B	0.626350	0.327840	0.525749	0.147
H(18)C	0.629533	0.425077	0.576307	0.147
N(3)	0.000000	0.5822(4)	0.750000	0.0551(14)
C(19)	0.9882(3)	0.5424(8)	0.6505(8)	0.063(3)
C(20)	0.9512(4)	0.4687(8)	0.6257(9)	0.074(3)
C(21)	0.9425(2)	0.4372(5)	0.5235(5)	0.107(2)
C(22)	0.9632(4)	0.6203(9)	0.7770(9)	0.079(3)
C(23)	0.9405(6)	0.7047(14)	0.7204(13)	0.129(6)
C(24)	0.9004(2)	0.7293(6)	0.7458(6)	0.121(3)
C(19)B	0.9790(4)	0.5001(9)	0.6814(9)	0.078(3)
C(20)B	0.9572(4)	0.5258(11)	0.5795(10)	0.096(4)
C(22)B	0.9660(4)	0.6619(9)	0.7360(9)	0.071(3)
C(23)B	0.9252(5)	0.6383(10)	0.7505(10)	0.096(4)

inorganic tetrahedral $[CoBr_4]^{2-}$ anions. The 3D network cohesion is ensured by hydrogen bonds between bromine atoms and hydrogen atoms of CH_3 groups. The distances and angles for anionic and cationic parts are summarized in Table 4. The Co–Br bond lengths vary from 2.403(1) to 2.433(1) Å with a mean value of 2.418 Å. The Br–Co–Br angle values are in the range of

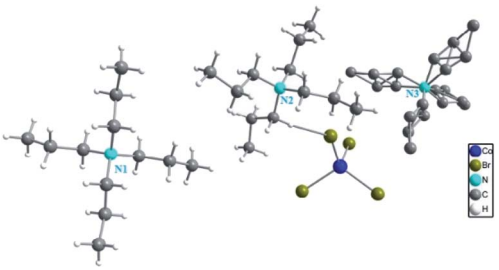

Fig. 2 Asymmetric unit of $[TPA]_2CoBr_4$ sample.

106.66(4)–112.51(3)° with the mean value of 109.585°. These values are close to those observed in the anionic part of $[C_4H_{12}N_2]CoBr_4$.[21]

The organic cations can adopt various geometries. The $[(C_3H_7)_4N(1)]^+$ cation has a cross-shaped conformation. The N–C and C–C bond lengths vary from 1.514(5) to 1.518(5) Å and from 1.498(7) to 1.517(7) Å, respectively. The C–N–C, C–C–N and C–C–C angles are in the range of 110.4(3)–110.6(3)°, 116.3(4)° and 110.0(5)–110.7(5)°, respectively. The $[(C_3H_7)_4\ N(2)]^+$ cation presents a broken cross-shaped conformation. For the second geometry, the N–C bond lengths vary from 1.506(6) to 1.529(6) Å. The C–C bond lengths vary from 1.471(8) to 1.537(8) Å. The C–N–C, N–C–C and C–C–C angles are in the range of 107.8(3)–111.3(4)°, 115.9(4)–117.4(4)° and 110.0(5)–111.3(5)°,

Table 3 Anisotropic displacement parameters (ADP, Å^2) of $[TPA]_2CoBr_4$

Atom	U_{11}	U_{22}	U_{33}	U_{23}	U_{13}	U_{12}
Co(1)	0.0535(4)	0.0522(4)	0.0647(4)	−0.0134(3)	0.0285(3)	−0.0097(3)
Br(1)	0.0651(4)	0.0728(4)	0.0889(4)	−0.0121(3)	0.0389(3)	0.0046(3)
Br(2)	0.0747(4)	0.0890(5)	0.0784(4)	−0.0241(3)	0.0206(3)	0.0179(3)
Br(3)	0.0897(4)	0.0758(4)	0.0925(5)	−0.0351(3)	0.0415(4)	−0.0330(3)
Br(4)	0.0821(4)	0.0795(4)	0.1058(5)	0.0051(3)	0.0494(4)	−0.0219(3)
N(1)	0.052(3)	0.045(3)	0.055(3)	0.000	0.021(3)	0.000
C(1)	0.050(3)	0.053(3)	0.060(3)	−0.009(2)	0.018(2)	−0.003(2)
C(2)	0.087(4)	0.069(4)	0.054(3)	−0.001(3)	0.022(3)	0.007(3)
C(3)	0.081(4)	0.108(5)	0.059(3)	−0.018(3)	0.019(3)	0.004(4)
C(4)	0.066(3)	0.055(3)	0.058(3)	−0.005(2)	0.028(3)	−0.013(3)
C(5)	0.061(3)	0.081(4)	0.093(4)	−0.016(3)	0.033(3)	−0.015(3)
C(6)	0.079(4)	0.118(6)	0.116(5)	−0.029(4)	0.055(4)	−0.041(4)
N(2)	0.054(2)	0.044(2)	0.049(2)	0.0000(18)	0.0250(19)	−0.0033(18)
C(7)	0.079(4)	0.053(3)	0.058(3)	−0.006(3)	0.027(3)	0.000(3)
C(8)	0.116(5)	0.092(5)	0.060(4)	0.003(3)	0.033(4)	0.001(4)
C(9)	0.203(9)	0.140(7)	0.056(4)	−0.012(4)	0.003(5)	−0.059(7)
C(10)	0.083(4)	0.049(3)	0.073(4)	0.004(3)	0.035(3)	0.007(3)
C(11)	0.078(4)	0.060(3)	0.085(4)	0.007(3)	0.034(3)	0.005(3)
C(12)	0.096(5)	0.073(4)	0.095(4)	0.011(3)	0.054(4)	0.023(3)
C(13)	0.054(3)	0.051(3)	0.059(3)	0.005(2)	0.024(2)	−0.006(2)
C(14)	0.067(4)	0.068(4)	0.073(4)	0.009(3)	0.024(3)	0.005(3)
C(15)	0.070(4)	0.082(4)	0.076(4)	0.021(3)	0.012(3)	0.004(3)
C(16)	0.082(4)	0.061(3)	0.078(4)	0.001(3)	0.043(3)	−0.017(3)
C(17)	0.101(5)	0.098(5)	0.125(6)	−0.029(4)	0.064(5)	−0.033(4)
C(18)	0.079(4)	0.085(5)	0.150(6)	−0.007(4)	0.065(5)	−0.023(4)
N(3)	0.055(3)	0.055(3)	0.064(4)	0.000	0.033(3)	0.000
C(21)	0.119(6)	0.119(6)	0.081(5)	−0.038(4)	0.034(4)	−0.027(5)
C(24)	0.088(5)	0.149(7)	0.121(6)	−0.026(5)	0.030(4)	0.058(5)

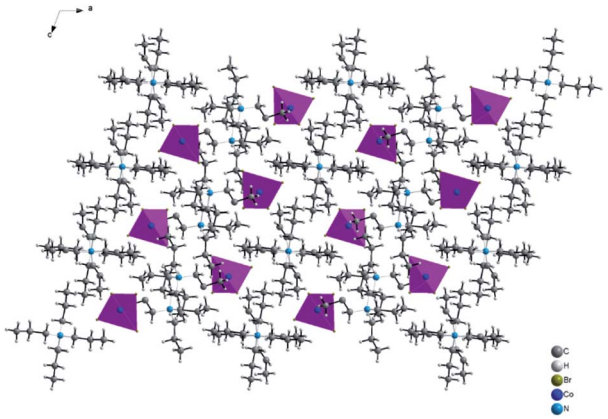

Fig. 3 Projection along *b* axis of the structural arrangement of $[TPA]_2CoBr_4$ sample.

respectively. For the third geometry, $[(C_3H_7)_4N(3)]^+$, the N–C and C–C bond lengths vary from 1.517(13) to 1.564(14) Å and from 1.48(2) to 1.559(17) Å, respectively. The C–N–C, N–C–C and C–C–C angles are in the range of 79.9(7)–140.5(7)°, 49.9(5)–170.0(17)° and 47.1(9)–156.9(13)°, respectively. These interatomic distances and angles are in good agreement with those observed previously in the cationic part of $[(C_3H_7)_4N]_2CoCl_4$,[15] $[(C_3H_7)_4N]_2Cu_2Br_6$ (ref. 22) and $[(C_3H_7)_4N]_2MnCl_4$.[23]

3.2. X-ray powder diffraction analysis

A part of the blue crystals thus formed has been crushed in order to check the sample homogeneity by recording X-ray powder diffraction pattern at room temperature. A refinement of the XRPD pattern collected at room temperature was carried out by the Le Bail method using the monoclinic cell parameters and the *C*2/*c* (*n*° 15) space group. Fig. 4 shows the observed, calculated, and difference diffraction patterns for $[TPA]_2CoBr_4$. All Bragg peaks were successfully indexed and satisfactorily modeled, thus confirming the high purity of the sample. The conventional reliability factors of the refinement are R_p = 8.04%, $R_{\omega p}$ = 9.55%, R_{exp} = 2.43%. The monoclinic cell parameters, a = 33.163(2) Å, b = 14.2356(9) Å, c = 15.0890(9) Å and β = 110.314(3)°, are in good agreement with those determined from XRD data collected on a single crystal of $[TPA]_2CoBr_4$.

3.3. Differential scanning calorimetric studies

In Fig. 5, one endothermic and one exothermic peak are observed in the DSC curve at 394 and 354 K on heating up and cooling down the sample at 10 K min^{-1}, respectively. A thermogravimetric analysis was carried out to probe the thermal stability of the sample. As shown in Fig. 5, no weight loss is measured in the temperature range 300–423 K. Since no thermal decomposition of the sample occurs up to 423 K, the $[TPA]_2CoBr_4$ compound therefore exhibits a reversible structural phase transition.

Table 4 Selected inter (Å) and angles (°) of $[TPA]_2CoBr_4$

Atom1–atom2	*d*, Å	Atom1–atom2	*d*, Å
Co(1)–Br4	2.4034(9)	C(11)–C(12)	1.501(7)
Co(1)–Br3	2.4137(9)	C(13)–C(14)	1.499(7)
Co(1)–Br2	2.4255(10)	C(14)–C(15)	1.514(7)
Co(1)–Br1	2.4330(9)	C(16)–C(17)	1.471(8)
N(1)–C(1)	1.514(5)	C(17)–C(18)	1.537(8)
N(1)–C(4)	1.518(5)	N(3)–C(22)	1.517(13)
C(1)–C(2)	1.504(7)	N(3)–C(19)	1.523(11)
C(2)–C(3)	1.517(7)	N(3)–C(19)B	1.558(14)
C(4)–C(5)	1.517(7)	N(3)–C(22)B	1.564(14)
C(5)–C(6)	1.498(7)	C(19)–C(20)	1.559(17)
N(2)–C(7)	1.506(6)	C(20)–C(21)	1.535(13)
N(2)–C(16)	1.508(6)	C(21)–C(20)B	1.505(16)
N(2)–C(13)	1.513(6)	C(22)–C(23)	1.51(2)
N(2)–C(10)	1.529(6)	C(23)–C(24)	1.55(2)
C(7)–C(8)	1.505(7)	C(24)–C(23)B	1.526(16)
C(8)–C(9)	1.507(9)	C(19)B–C(20)B	1.500(19)
C(10)–C(11)	1.496(7)	C(22)B–C(23)B	1.48(2)

Atom1–atom2–atom3	Angle (°)	Atom1–atom2–atom3	Angle (°)
Br(4)–Co(1)–Br(3)	108.83(4)	C(22)B–N(3)–C(22)B	86.8(10)
Br(4)–Co(1)–Br(2)	106.66(4)	C(19)B–C(19)–C(20)B	89.4(15
Br(3)–Co(1)–Br(2)	109.64(4)	C(19)B–C(19)–N(3)	75.6(12)
Br(4)–Co(1)–Br(1)	109.27(4)	C(20)B–C(19)–N(3)	141.7(11)
Br(3)–Co(1)–Br(1)	109.83(3)	C(20)B–C(19)–C(20)	46.1(8)
Br(2)–Co(1)–Br(1)	112.51(3)	N(3)–C(19)–C(20)	113.6(9)
C(1)–N(1)–C(1)	107.5(5)	C(19)B–C(19)–C(22)	117.8(14)
C(1)–N(1)–C(4)	110.4(3)	C(20)B–C(19)–C(22)	151.8(12)
C(1)–N(1)–C(4)	110.6(3)	N(3)–C(19)–C(22)	49.9(5)
C(1)–N(1)–C(4)	110.6(3)	C(20)–C(19)–C(22)	161.3(10)
C(1)–N(1)–C(4)	110.4(3)	C(19)B–C(20)–C(20)B	84.3(13)
C(4)–N(1)–C(4)	107.4(5)	C(19)B–C(20)–C(21)	134.5(13
C(2)–C(1)–N(1)	116.3(4)	C(20)B–C(20)–C(21)	66.7(10)
C(1)–C(2)–C(3)	110.7(5)	C(20)B–C(20)–C(19)	51.2(9)
C(5)–C(4)–N(1)	116.3(4)	C(21)–C(20)–C(19)	107.3(9)
C(6)–C(5)–C(4)	110.0(5)	C(22)B–C(22)–C(23)B	88.7(16
C(7)–N(2)–C(16)	108.9(4)	C(23)B–C(22)–C(23)	52.4(10)
C(7)–N(2)–C(13)	109.5(3)	C(22)B–C(22)–N(3)	76.2(14)
C(16 N(2)–C(13)	111.3(4)	C(23)B–C(22)–N(3)	146.2(13)
C(7)–N(2)–C(10)	110.8(4)	C(23)–C(22)–N(3)	114.9(13)
C(16)–N(2)–C(10)	108.6(4)	C(22)B–C(22)–C(19)	120.4(16)
C(13)–N(2)–C(10)	107.8(3)	C(23)B–C(22)–C(19)	150.4(14)
C(8)–C(7)–N(2)	115.9(4)	C(23)–C(22)–C(19)	156.9(13)
C(7)–C(8)–C(9)	110.7(5)	N(3)–C(22)–C(19)	50.2(5)
C(11)–C(10)–N(2)	116.6(4)	C(22)B–C(23)–C(23)B	82.4(18)
C(10)–C(11)–C(12)	111.3(5)	C(23)B–C(23)–C(22)	51.0(11)
C(13)–C(14)–C(15)	110.0(5)	C(22)B–C(23)–C(24)	144(2)
C(17)–C(16)–N(2)	117.4(4)	C(23)B–C(23)–C(24)	65.4(12)
C(16)–C(17)–C(18)	110.7(5)	C(22)–C(23)–C(24)	109.9(14)
C(22)–N(3)–C(22)	138.0(11)	C(23)B–C(24)–C(23)	47.3(8)
C(22)–N(3)–C(19)	79.9(7)	C(19)–C(19)B–C(20)	103.1(16)
C(22)–N(3)–C(19)	116.3(6)	C(19)–C(19)B–C(20)B	54.7(12)
C(22)–N(3)–C(19)	116.3(6)	C(20)–C(19)B–C(20)B	48.7(9)
C(22)–N(3)–C(19)	79.9(7)	C(19)–C(19)B–N(3)	71.3(12)
C(19)–N(3)–C(19)	136.3(10)	C(20)–C(19)B–N(3)	150.9(13)
C(22)–N(3)–C(19)B	107.9(7)	C(20)B–C(19)B–N(3)	116.3(11)
C(22)–N(3)–C(19)B	103.4(7)	C(20)–C(20)B–C(19)	82.7(13)
C(19)–N(3)–C(19)B	106.2(8)	C(20)–C(20)B–C(19)B	47.1(9)
C(22)–N(3)–C(19)B	103.4(7)	C(20)–C(20)B–C(21)	69.5(11)
C(22)–N(3)–C(19)B	107.9(7)	C(19)–C(20)B–C(21)	131.6(13)
C(19)–N(3)–C(19)B	106.2(8)	C(19)B–C(20)B–C(21)	108.5(1)
C(19)B–N(3)–C(19)B	82.6(10)	C(22)–C(22)B–C(23)	107(2)
C(22)–N(3)–C(22)B	108.3(8)	C(22)–C(22)B–C(23)B	54.6(12)

Table 4 (*Contd.*)

Atom1–atom2–atom3	Angle (°)	Atom1–atom2–atom3	Angle (°)
C(19)–N(3)–C(22)B	102.1(6)	C(23)–C(22)B–C(23)B	55.6(13)
C(19)–N(3)–C(22)B	109.3(6)	C(22)–C(22)B–N(3)	70.4(13)
C(19)B–N(3)–C(22)B	108.7(6)	C(23)–C(22)B–N(3)	170.0(17)
C(19)B–N(3)–C(22)B	140.5(7)	C(23)B–C(22)B–N(3)	117.9(11)
C(22)–N(3)–C(22)B	108.3(8)	C(22)–C(23)B–C(23)	76.6(14)
C(19)–N(3)–C(22)B	109.3(6)	C(22)–C(23)B–C(24)	132.8(14)
C(19)–N(3)–C(22)B	102.1(6)	C(23)–C(23)B–C(24)	67.4(13)
C(19)B–N(3)–C(22)B	140.5(7)	C(22)B–C(23)B–C(24)	107.8(11)
C(19)B–N(3)–C(22)B	108.7(6)		

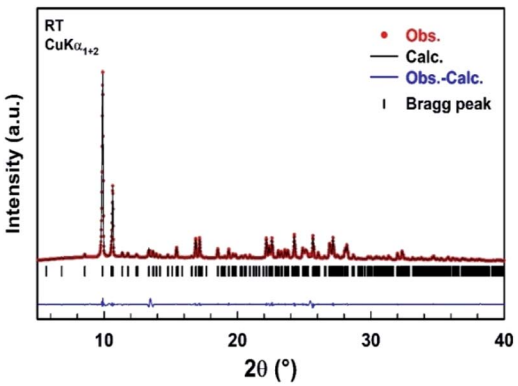

Fig. 4 Comparison of the observed diffraction pattern of $[TPA]_2CoBr_4$ compound (red dots) with the pattern calculated by the Le Bail method (black line). The blue curve corresponds to the difference between observed and calculated patterns. Vertical markers give Bragg peak positions of the monoclinic space group *C*2/*c* (no. 15). The two peaks at $2\theta = 13.5°$ and $2\theta = 25.5°$ of very low intensity are attributed to an unknown impurity.

The enthalpy and the entropy variations of the transition are 2.41 kJ mol^{-1} and 6.11 J mol^{-1} K^{-1} respectively. The type of phase transition can be deduced by the Boltzmann function:

$$\Delta S = k_B \ln(\Omega) \quad (1)$$

where k_B is Boltzmann constant and Ω is the ratio of distinguishable orientations in the high and the low temperature phases $\left(\Omega = \frac{N1}{N2}\right)$. The obtained value of Ω is greater than 2 indicating that the phase transition can be classified as an order–disorder type.[24]

3.4. Vibrational spectroscopy

The infrared and the Raman spectra of the $[TPA]_2CoBr_4$ were recorded at room temperature and shown in Fig. 6. The assignment of the internal vibrations modes is based on a comparison with other spectra of homologous compounds.[23,25]

The main intensity bands observed in the low wavenumbers region are attributed to the four fundamental vibrational modes of $[CoBr_4]^{2-}$ anion. The bands at 55 cm^{-1} and 85 cm^{-1} are thus respectively assigned to the symmetric (ν_2) and asymmetric (ν_4) Br–Co–Br bending modes. The symmetric (ν_1) and asymmetric (ν_3) Co–Br stretching modes are observed at 161 and 308 cm^{-1}, respectively.

The bands corresponding to the vibrational modes of the cationic groups are observed at higher wavenumbers. The bands observed between 2800 and 3100 cm^{-1} are commonly assigned to the symmetric and asymmetric vibration of CH_2 and CH_3 groups.[26] The symmetric and asymmetric CH_3 stretching modes are attributed to the IR bands observed at 2903 and 2970 cm^{-1} (2969 cm^{-1} in Raman spectrum) respectively and the symmetric and asymmetric CH_2 stretching modes are attributed to the IR bands located at 2878 cm^{-1} (2875 cm^{-1} in Raman spectrum) and 2936 cm^{-1} (2932 cm^{-1} in Raman spectrum), respectively.

The intense IR bands located in the 1420–1500 cm^{-1} region are likely assigned to CH_2 scissoring modes, and the IR band at 1379 cm^{-1} to the CH_3 bending mode. The stretching (C–C–C) mode appears between 1015 and 1050 cm^{-1} in both Raman and IR spectra and the IR bands located in the 950–100 cm^{-1} region are attributed to the deformation δ(C–N–C) and δ(C–C–C)

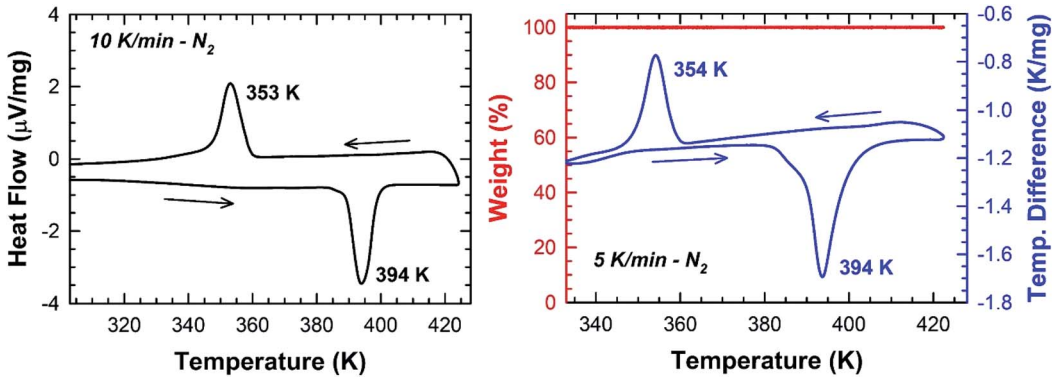

Fig. 5 DSC and TGA/DTA thermogram collected under N_2 on crushed blue crystals of $[TPA]_2CoBr_4$.

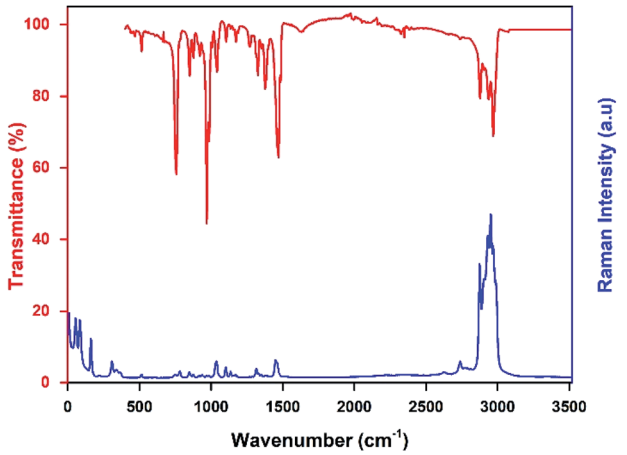

Fig. 6 Raman and infrared spectra of the $[TPA]_2CoBr_4$ compound collected at room temperature.

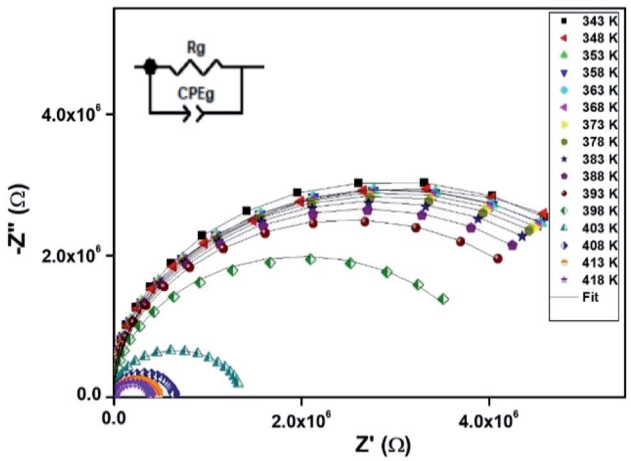

Fig. 7 Nyquist representation of observed complex impedance spectra (dots) collected on a dense pellet of the $[TPA]_2CoBr_4$ compound.

modes. Finally, the intense infrared bands centered at 758 cm^{-1} are mainly attributed to $\nu_1(NC_4)$ modes of the $[(C_3H_7)_4N]^+$cation (Fig. 7).

3.5. Impedance analysis

The electrical properties were studied by the non-destructive complex impedance method. Fig. 6 shows the Nyquist diagrams ($-Z''$ *versus* Z') of the $[TPA]_2CoBr_4$ compound at different temperatures (343–418 K).

All impedance spectra show some dispersion instead of a semicircle centered on the real axis, indicating a non-Debye (Cole–Cole) type relaxation.[27,28] As the temperature increases, the radius of the semicircle and the associated grain resistance value progressively decrease, confirming the negative temperature coefficient of resistance (NTCR) and a signature of the semiconductor character.[29] The best fit using Zview software (black solid line in Fig. 6) was obtained using an equivalent circuit formed by a parallel combination of bulk resistance R_g and fractal capacity CPE_g.

Fits are performed by using Z-view2 software[30] (black solid line in Fig. 6). The impedance of the constant phase element (Z_{CPE}) is determined from the formula:[31]

$$Z_{CPE} = \frac{1}{Qj\omega^n} \quad (2)$$

where Q indicates the value of the pseudo-capacitance of the CPE element and the exponent n determines the phase angle $\beta = n\pi/2$ between the radius of the semicircle and the Z' axis in the Nyquist representation. It is assumed that CPE depicts an ideal resistor for n equal to 0 while for $n = 1$ represent an ideal capacitance.[32]

The real Z' and imaginary Z'' parts of impedance of the equivalent circuit were fitted using the following formula:[31]

$$Z' = \frac{R_g\left(1 + R_g A_0 \omega^n \cos(\beta)\right)}{\left(1 + R_g A_0 \omega^n \cos(\beta)\right)^2 + \left(R_g A_0 \omega^n \sin(\beta)\right)^2} \quad (3)$$

$$-Z'' = \frac{{R_g}^2 A_0 \omega^n \sin(\beta)}{\left(1 + R_g A_0 \omega^n \cos(\beta)\right)^2 + \left(R_g A_0 \omega^n \sin(\beta)\right)^2} \quad (4)$$

The extracted parameters of the equivalent circuit elements (R, Q and n) are summarized in Table 5. According to the calculated capacitance value the semicircle can be therefore assigned to the response of grains. Fig. 8 and 9 show the variation of the obtained values of R_g and CPE_g with temperature respectively. The grain resistance (R_g) slightly decreases upon heating until $T = 394$ K before it drops sharply at the transition temperature. This decrease in the resistive property with increasing the temperature indicating the existence of activated conduction mechanism. The obtained values of bulk resistance (R_g), corresponding to the grain, are used to determine the electrical conductivity σ_g as follows:[31]

Table 5 Electrical fitted circuit parameters for $[TPA]_2CoBr_4$ at different temperatures

T (K)	R_g (10^6 Ω)	CPE_g (10^{-10} F)	Exponent n
343	6.14	1.41	0.99
348	5.96	1.42	0.99
353	5.91	1.43	0.99
358	5.90	1.43	0.98
363	5.88	1.46	0.97
368	5.83	1.46	0.997
373	5.77	1.47	0.96
378	5.68	1.47	0.94
383	5.54	1.48	0.96
388	5.33	1.49	0.97
393	5.02	1.50	0.95
398	4.01	1.58	0.99
403	1.34	1.68	0.99
408	0.64	1.76	0.98
413	0.48	1.78	0.98
418	0.39	1.80	0.97

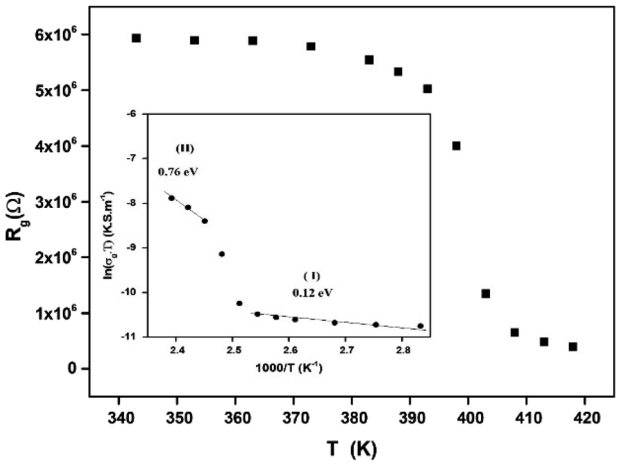

Fig. 8 Variation of the grain resistance R_g with temperature.

$$\sigma_g = \frac{e}{S_1 * R_g} \quad (5)$$

where e is the thickness of the sample, S_1 is the area of one flat face of the pellet. The thermal dependence of R_g and the electrical conductivity $\ln(\sigma_g T)$ *versus* $(1000/T)$ are displayed in Fig. 8. The conductivity slightly increases in a linear fashion in the temperature range 300–393 K (region I) before suddenly jumps above 393 K. Above 408 K, a second linear regime of conduction starts (region II). This conductivity jump occurs at the temperature for which a structural phase transition has been detected by DTA analysis (Fig. 5). In the two linear regimes, the conductivity obeys a law of Arrhenius type:

$$\sigma_g T = \sigma_0 \exp\left(-\frac{E_a}{k_B T}\right) \quad (6)$$

where σ_0 is pre-exponential conductivity term, k_B is the Boltzmann constant and E_a is the activation energy. The activation energies calculated (least squares linear regressions) from the linear temperature dependence of the conductivity in regions I and II are E_a (I) = 0.12 eV and E_a (II) = 0.76 eV, respectively. These values are comparable to those found for other organic–inorganic semiconductors.[15,21]

In Fig. 9, one can note that the capacitance CPE_g suddenly increases at the structural phase transition (T = 394 K). Moreover, such variation can be related to an ionization process beyond transition temperature which decreases the resistance (by increasing the density and the mobility of free charge carriers) and increases the capacitance (by increasing the space charge).

Fig. 10 displays the variation of the real part (Z') of the impedance with frequency at different temperatures. At low frequencies, Z' is independent of temperature until 394 K. Then it is observed that beyond 394 K, the value of Z' decreases on increasing temperature, which can be explained by the reduction of trapped charge density and a thermal activation of their mobility.[33] As frequency increases, the real impedance Z' increases until a specific frequency for each temperature.

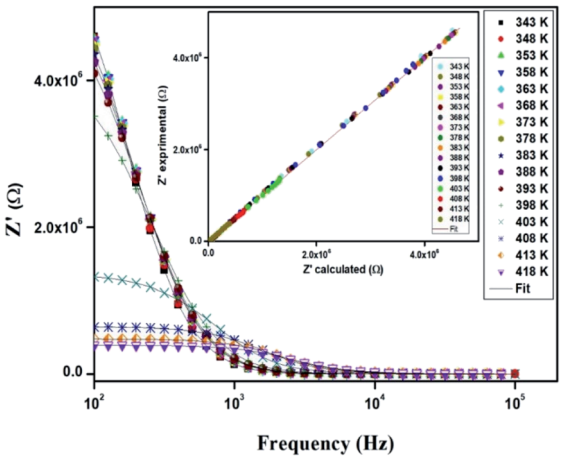

Fig. 10 Variation of the real part (Z') of impedance as a function of the frequency for different temperatures.

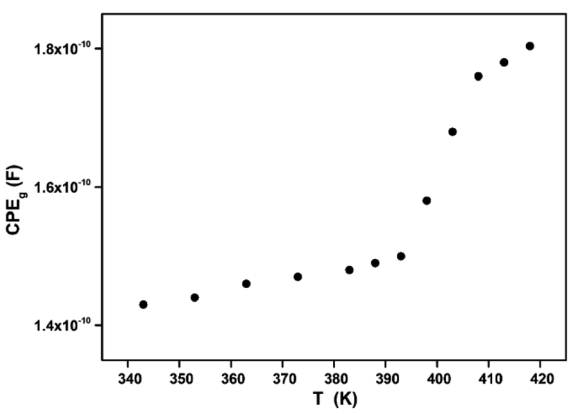

Fig. 9 Variation of the grain fractal capacitance CPE_g with temperature.

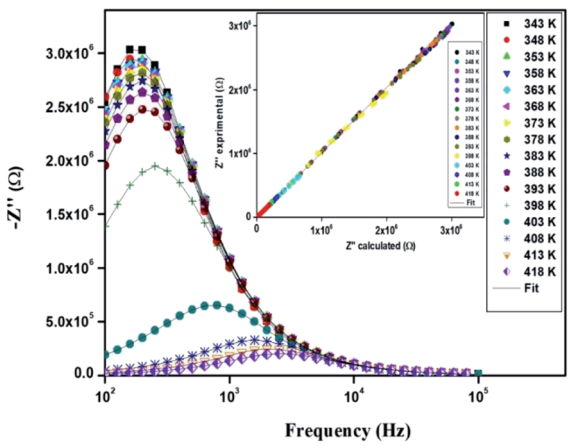

Fig. 11 Variation of the imaginary part (Z'') of impedance as a function of the frequency for different temperatures.

Besides, the values of Z′ merge at high frequencies (>10^4 Hz). This can be understood by the fact that charge carriers acquired sufficient energy to overcome the potential barrier.[34,35]

The variation of the imaginary part (Z'') as the function of frequency for different temperatures is shown in Fig. 11. Let us note that the plot below 394 K is slightly increased with increasing temperature. However, the frequency (f_{max}), at which the imaginary value Z'' has the highest value (Z''_{max}), shifts to high frequencies as the temperature increases above 394 K, thus confirming the occurrence of non-Debye relaxation type.[36] Further, we notice a peak broadening with decreasing of the value of Z''_{max} which suggests an increasing loss in the resistive properties of the sample.[37] The relaxation peak shifts to high frequency regions indicating the accumulation of space charge in the material.[38]

In order to compare the experimental and theoretical results (using an equivalent circuit), the experimental data of Z' and Z'' *versus* the simulated ones were also plotted in Fig. 10 and 11. The straight lines, with a slope equal to the unity, prove the very good agreement between the experimental and theoretical data. This behavior confirms moreover that the modeled equivalent circuit describes well the electric properties of our compound.[39]

3.6. Electric modulus analysis

The analyses of the electrical modulus provide an insight about the electrode polarization and relaxation times of the conductivity.[40] The complex electric modulus M^* is represented by:

$$M^* = \frac{1}{\varepsilon^*} = j\omega C_0 Z^* = M' + jM'' \quad (7)$$

where, C_0 is the vacuum capacitance. Fig. 12 represents the frequency dependence of the imaginary part (M'') of the modulus at different temperatures. It is observed that the peak maximum M''_{max} shifts to higher frequencies with increasing temperature. This indicates that the dielectric relaxation process is thermally activated in which the hopping process of charge carriers overcomes intrinsically.[29,41] This behavior confirms that the relaxation is non-Debye type (single relaxation time).[42] Fig. 13 shows the complex modulus spectrum (M'' *versus*

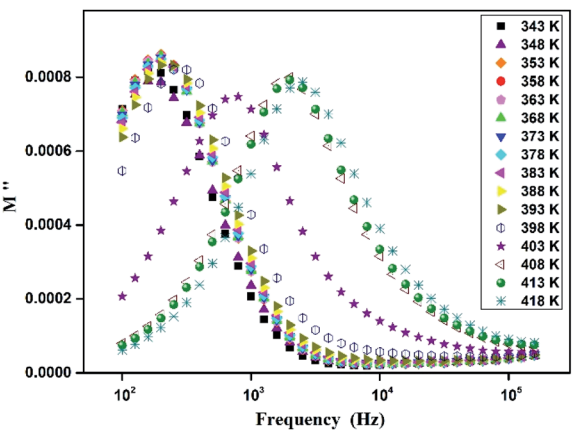

Fig. 12 Frequency dependence of the M'' modulus at different temperatures.

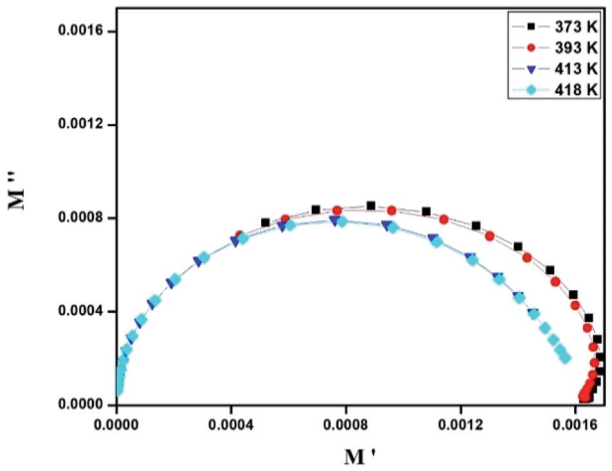

Fig. 13 Complex modulus spectrum of $[TPA]_2CoBr_4$ at selected temperatures.

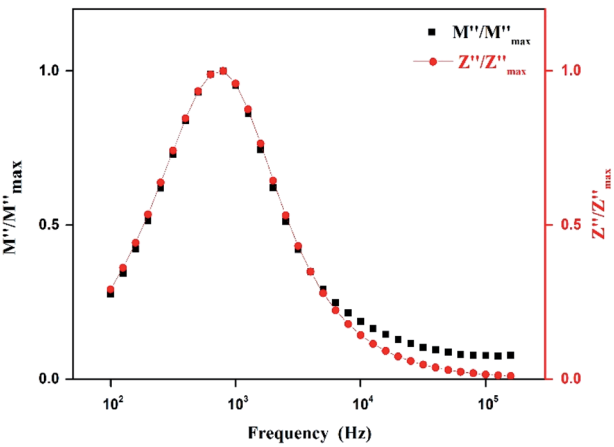

Fig. 14 Logarithmic plot of normalized parameters (M'', Z'') of $[TPA]_2CoBr_4$ measured at selected temperature.

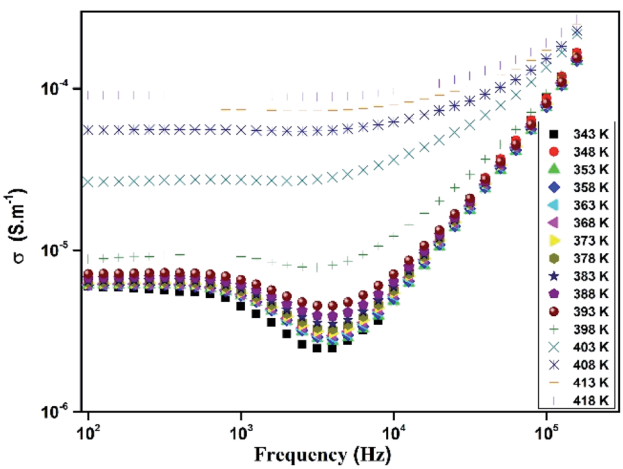

Fig. 15 Frequency dependence of total conductivity at different temperatures.

M') of $[TPA]_2CoBr_4$ at selected temperatures. It exhibits a single semicircular arc where the intercept with the real axis indicates the capacitive contribution of the grains. Also, it confirms that the effect of bulk boundaries is negligible. Here, the existence of non-semicircles in plot M'' *versus* M' proves non-Debye-type relaxation.[43] The plots behavior shows a marked change in its shape upon heating above 394 K suggesting the probable change in the capacitance values of the material.[44] This behavior confirms the presence of the phase transition detected by the thermal analysis.

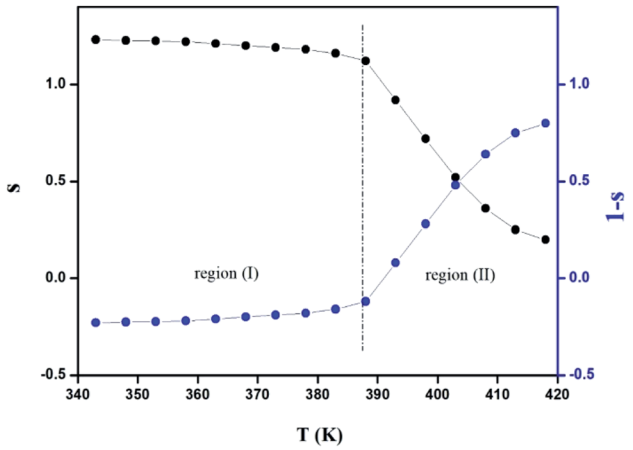

Fig. 16 Variation of the exponent s (and $1 - s$) of the Jonscher's power law with the temperature.

Fig. 14 shows the variation of the imaginary part of electric modulus M'' and the imaginary part of impedance Z'' as the frequency F increases at 403 K. In this figure, both curves exhibit a maximum at the same frequency value. This superimposition is characteristic of a long range electronic conductivity within grains[45] which is responsible for the high-temperature dielectric relaxation observed.[46,47]

3.7. Ac conductivity

The variation of total conductivity σ for $[TPA]_2CoBr_4$ *versus* frequencies at different temperatures is shown in Fig. 15. At low frequencies, the spectrum exhibits a plateau region (independent of frequency) which is related to the direct current conductivity σ_{dc}. On further increase of temperature (above 394 K), an increase of conductivity is established in the graph indicating that electrical conductivity is thermally activated. This behavior suggests the semiconductor nature of this compound. Below the phase transition temperature 394 K, charge carriers are emitted in grains and are blocked at grain boundaries. The conductivity decreases with frequency and reaches a minimum until a frequency f_{hop} at which charge carriers can hop over grain boundary barrier. Above 394 K

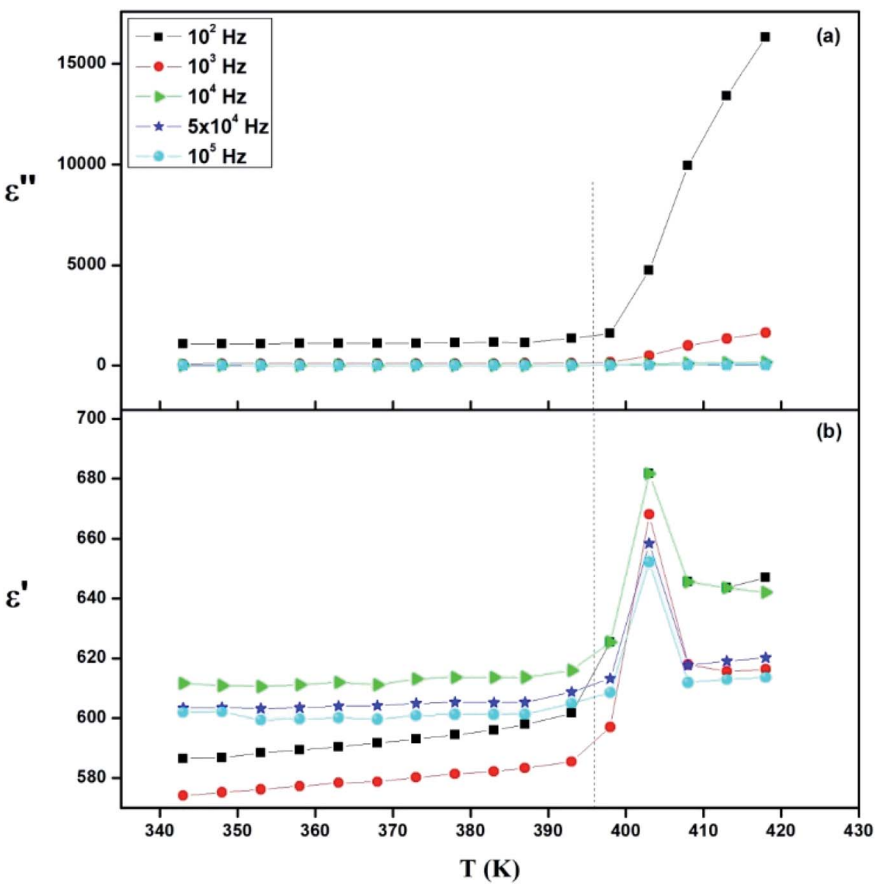

Fig. 17 Thermal evolution of (a) relative permittivity (ε') and (b) dielectric loss (ε'') at different frequencies.

charge carriers have enough thermal energy to avoid accumulation at grain boundaries. It is also observed a decay of this phenomenon with an increase of temperature (above 394 K). Beyond f_{hop}, the conductivity increases with an increase of frequency, which is related to the alternative current conductivity σ_{ac}. Then at low frequency, the conductivity merges with direct current one σ_{dc} and at high frequency, it follows the Jonscher's law expressed by:[48]

$$\sigma = A_1\omega^s \quad (8)$$

where, A_1 is a constant, ω is the angular frequency ($\omega = 2\pi f$), s is a coefficient expressing the degree of interaction between the mobile charge and its surrounding.

The variation of the high frequency exponent 's' (Fig. 16) allows to determine the conduction mechanism subjected to an alternating voltage.[49] The plot of the exponent 's' shows two distinct regions; below 394 K, a plateau region (independent of temperature) is observed indicating the quantum mechanical tunneling (QMT) model (region I).[50] Then the exponent 's' decreases with an increase of temperature. This behavior is a signature of the correlated barrier hopping model (CBH) of the electrical transport[51] (region II). The value of the potential barrier W_M is deduced from the linear fit of the curve $(1 - s)$ *versus* temperature (Fig. 17) using the following equation:

$$s = 1 - \frac{6k_BT}{W_M - k_BT\ln(\omega\tau_0)} \quad (9)$$

where τ_0 is the characteristic relaxation time. At higher binding energy, 's' can be written in the following form:[52]

$$s = 1 - \frac{6k_BT}{W_M} \quad (10)$$

The obtained value of W_M is 0.25 eV.

3.8. Dielectric measurement

The dielectric measurement is a powerful characterization technique to obtain information about conduction behavior and to determine the origin of dielectric loss and dipolar relaxation time.[53]

Fig. 17 presents the temperature dependence plots of the real ε' and ε'' imaginary part of the complex dielectric response ε^* of the $[TPA]_2CoBr_4$ compound at selected frequencies. Such variation indicates that the compound undergoes a phase transition at the same temperature as that deduced from thermal and electrical analyses. It is clearly observed that the dielectric parameters (both of the ε' and ε'') below 394 K are independent of temperature. Beyond 394 K, ε' and ε'' increase as the temperature rises until $T = 403$ K. This behavior can be explained by orientational polarization where dipoles align themselves along the electric field direction and fully contribute to the total polarization.[54–56] Also, the variation of ε' shows a peak at a critical transition temperature $T_c = 403$ K. As the temperature increases, the dipoles follow the variation of the field which becomes too rapid so the real value of ε' decreases.[57,58] Furthermore, there is no displacement of the dielectric maximum with the increase in frequency, thus confirming that the dielectric constant has a classical thermal evolution.[59,60]

4. Conclusion

In this work, a new $[TPA]_2CoBr_4$ compound, with a monoclinic symmetry and $C2/c$ space group, was prepared and its optical, thermal, electrical and dielectric properties are investigated as a function of temperature and frequency. One reversible structural phase transition at $T = 394$ K is detected from thermal and electrical analyses. The Nyquist plot reveals the presence of grain contributions and allowed determining an equivalent circuit formed by a single R//CPE. The variation of the extracted parameters values R_g and CPE_g confirms the existence of a structural phase transition at $T = 394$ K. The analysis of electrical modulus confirms the presence of phase transition and shows the non-Debye relaxation process. The ac conductivity has been studied as a function of temperature at different temperature. It confirms the presence of the phase transition deduced by the DSC analysis. The variation of the frequency exponent s with temperature confirms that the correlated barrier hopping is the dominant transport mechanism at high temperature in this compound. Modulus and capacitance analyses prove the high effective permittivity at radio frequencies in the sample. The dielectric analysis shows a high maximum of ~680 and also confirms that the compound undergoes a phase transition at the same temperature as that deduced from thermal and electrical analyses.

Conflicts of interest

All authors have no conflicts of interest.

References

1 K. E. Lee, N. Morad, T. T. Teng and B. T. Poh, *Chem. Eng. Sci.*, 2012, **203**, 370–386.
2 F. Garnier, *Chem. Phys.*, 1998, **227**, 253–262.
3 A. Gagor, M. Wojtas, A. Pietraszko and R. Jakubas, *Acta Crystallogr., Sect. B: Struct. Sci.*, 2008, **64**, 558–566.
4 M. W. Urban, *Handbook of Stimuli Responsive Materials* 2011.
5 M. A. Stuart, W. T. Huck, J. Genzer, M. Müller, C. Ober, M. Stamm, G. B. Sukhorukov, I. Szleifer, V. V. Tsukruk, M. Urban and F. Winnik, *Nat. Mater.*, 2010, **9**, 101–113.
6 S. Horike, S. Shimomura and S. Kitagawa, *Nat. Chem.*, 2009, **9**, 695–704.
7 S. Horiuchi and Y. Tokura, *Nat. Mater.*, 2008, **7**, 357–366.
8 O. Sato, J. Tao and Y. Z. Zhang, *Angew. Chem., Int. Ed.*, 2007, **46**, 2152–2157.
9 Z. H. Sun, J. H. Luo, T. L. Chen, L. N. Li, R. G. Xiong, M. L. Tong and M. C. Hong, *Adv. Funct. Mater.*, 2012, **22**, 4855–4861.
10 G. Amirthaganesan, M. A. Kandaswamy and M. Dhandapani, *Mater. Chem. Phys.*, 2008, **110**, 328–331.
11 K. Karoui, A. Ben Rhaiem, F. Hlel, M. Arous and K. Guidara, *Mater. Chem. Phys.*, 2012, **133**, 1–7.

12 eslati, I. Chaabane and F. Hlel, *Vib. Spectrosc.*, 2014, **73**, 116–126.
13 K. Ben Brahim, M. Ben gzaiel, A. Oueslati, F. Hlel and M. Gargouri, *Mater. Res. Bull.*, 2019, **118**, 110505.
14 M. Asplund and S. Jagner, *Acta Chem. Scand., Ser. A*, 1984, **38**, 411–414.
15 N. Moutia, A. Oueslati, M. Ben Gzaiel and K. Khirouni, *Physica E*, 2016, **83**, 88–94.
16 R. Lim, *AIP Adv.*, 2016, **6**, 035307.
17 I. Chaabane, F. Hlel, K. Guidara and M. Gargouri, *J. Alloys Compd.*, 2008, **461**, 495–500.
18 H. A. Jahn and E. Teller, *Stat. Proc. Roy. Soc*, 1937, **161**, 220–235.
19 R. Megha, S. Kotresh, Y. T. Ravikiran, C. V. Ramana, S. C. Vijaya Kumari and S. Thomas, *Compos. Interfaces*, 2017, **24**, 55–68.
20 M. Naveed, M. Mumtaz, R. Khan, A. A. Khan and M. N. Khan, *J. Alloys Compd.*, 2017, **712**, 696–703.
21 H. Tllili, S. Walha, S. Elleuch, B. F. Ali and H. Naïli, *J. Mol. Struct.*, 2018, **1152**, 303–310.
22 A. Oueslati and M. Gargouri, *J. Alloys Compd.*, 2017, **739**, 1089–1096.
23 M. B. Gzaiel, A. Oueslati, F. Hlel and M. Gargouri, *Physica E*, 2016, **83**, 405–413.
24 W. Trigui, A. Oueslati, I. Chaabane, G. Corbel and F. Hlel, *Appl. Phys. A*, 2015, **119**, 673–680.
25 N. Moutia, M. Ben Gzaiel, A. Oueslati and K. Khirouni, *J. Mol. Struct.*, 2017, **1134**, 697–705.
26 J.-F. Bardeau, A. N. Parikh, J. D. Beers and B. I. Swanson, *J. Phys. Chem. B*, 2000, **104**, 627–635.
27 K. S. Cole and R. H. Cole, *J. Chem. Phys.*, 1941, **9**, 341–351.
28 H. Ferjani, H. Boughzala and A. Driss, *J. Crystallogr.*, 2013, **2013**, 1–8.
29 L. H. Omari, R. Moubah, A. Boutahar, L. Hajji and R. El Ouatib, *J. Electroceram.*, 2020, **44**, 23–31.
30 D. Johnson, *A High Measurement Channel Density Impedance Array Analyser: Instrumentation and Implementation Approaches*, Scribner Associates Inc, 150 E. Connecticut Avenue, Southern Pines, NC, USA., 2010, vol. 25, pp. 35–48.
31 M. Hamdi, A. Oueslati, I. Chaabane and F. Hlel, *Int. Scholarly Res. Not.*, 2012, 1–8.
32 F. Rehman, Li. Jing-Bo, J. S. Zhang, M. Rizwan, C. Niu and H. B. Jin, *J. Appl. Phys.*, 2015, **118**, 214101–214106.
33 K. Omri, R. Lahouli and L. El Mir, *Results Phys.*, 2019, **12**, 2141–2145.
34 M. J. Miah and A. K. M. Akther Hossain, *Acta Mater.*, 2016, **29**, 505–517.
35 V. Purohit, R. Padhee and R. N. P. Choudhary, *Ceram. Int.*, 2018, **44**, 3993–3999.
36 M. Ram, *Solid State Sci.*, 2010, **12**, 350–354.
37 P. Ganguly, A. K. Jha and K. L. Deori, *Solid State Commun.*, 2008, **146**, 472–477.
38 B. Behera, P. Nayak and R. N. P. Choudhary, *J. Alloys Compd.*, 2007, **436**, 226–232.
39 H. Nefzi, F. Sediri, H. Hamzaoui and N. Gharbi, *Mater. Res. Bull.*, 2013, **48**, 1978–1983.
40 P. S. Anantha and K. Hariharan, *Mater. Sci. Eng., B*, 2005, **121**, 12–19.
41 K. Sundaramahalingam, D. Vanitha, N. Nallamuthu, A. Manikandan and M. Muthuvinayagam, *Phys. Rev. B: Condens. Matter*, 2019, **553**, 120–126.
42 R. Gajula, L. R. Buddiga, K. C. Kumar and M. Dasari, *Results Phys.*, 2020, **17**, 103076.
43 S. Mohanta, I. Naik, S. D. Kaushik, S. Mukherjee and P. Patra, *J. Electron. Mater.*, 2019, **49**, 842–847.
44 Behera, N. K. Mohanty, B. Behera and P. Nayak, *Adv. Tapis. Lett*, 2013, **4**, 141–145.
45 D. C. Sinclair and A. R. West, *J. Appl. Phys.*, 1989, **66**, 3850–3856.
46 X. He, F. Han, M. Liu, Z. Yuan, X. Jiang, C. Hu, S. Ren, X. Lei and L. Liu, *J. Electron. Mater.*, 2020, **49**, 6643–6655.
47 S. I. R. Costa, M. Li, J. R. Frade and D. C. Sinclair, *RSC Adv.*, 2013, **3**, 7030–7036.
48 A. K. Jonscher, *Nature*, 1974, **250**, 191–193.
49 A. K. Jonscher, *Nature*, 1977, **267**, 673–679.
50 Y. B. Taher, A. Oueslati, N. K. Maaloul, K. Khirouni and M. Gargouri, *Appl. Phys. A*, 2015, **120**, 1537–1543.
51 I. G. Austin and N. F. Mott, *Adv. Phys.*, 1969, **18**, 41–102.
52 S. R. Elliott, *Philos. Mag. B*, 1977, **36**, 1291–1304.
53 S. Nasri, M. Megdiche and M. Gargouri, *Phys. E*, 2016, **16**, 30191–30196.
54 R. Ayouchi, D. Leien, F. Martin, M. Gabas, E. Dalchiele and J. R. Ramos-Barrodo, *Thin Solid Films*, 2003, **426**, 68–77.
55 V. Purohit, R. Padhee and R. N. P. Choudhary, *Ceram. Int.*, 2018, **44**, 3993–3999.
56 A. Ansari Sajid, N. Ambreen, F. Bushara, W. Khan, M. Chaman, A. Azam and A. H. Naqvi, *Mater. Res. Bull.*, 2012, **47**, 4161–4168.
57 W. Trigui, A. Oueslati, I. Chaabane and F. Hlel, *Ionics*, 2014, **20**, 231–241.
58 R. Lahouli, J. Massoudi, M. Smari, H. Rahmouni, K. Khirouni, E. Dhahrib and L. Bessaisd, *RSC Adv.*, 2019, **9**, 19949–19964.
59 A. Salhi, S. E. Sayouri, B. Jaber and L. H. Omari, *Appl. Phys. A*, 2018, **124**, 1–9.
60 L. H. Omari, L. Hajji, T. Lamhasni and C. Jama, *Mater. Chem. Phys.*, 2018, **223**, 60–67.